

Still-camera multiview Spectral Optical Flow Imaging for 3D operating-deflection-shape identification

Domen Gorjup^a, Janko Slavič^{a,*}, Aleš Babnik^a, Miha Boltežar^a

^aUniversity of Ljubljana, Faculty of Mechanical Engineering, Aškerčeva 6, 1000
Ljubljana, Slovenia

Cite as:

*Domen Gorjup, Janko Slavič, Aleš Babnik, Miha Boltežar,
Still-camera multiview Spectral Optical Flow Imaging for 3D
operating-deflection-shape identification, Mechanical Systems and
Signal Processing, Volume 152, 2021, 107456, ISSN 0888-3270,
<https://doi.org/10.1016/j.ymsp.2020.107456>.*

Abstract

To measure high-frequency 3D vibrations, multi-camera, high-speed imaging hardware is normally required. An alternative using still-frame cameras was recently introduced with the Spectral Optical Flow Imaging (SOFI) method. In this research, the SOFI method is extended to multiview measurements of spatial operating deflection shapes. This is achieved by utilizing harmonically controlled illumination to perform an analogue Fourier transform on image-intensity data in multiple camera views. The obtained multiview displacement spectra are combined with geometrical data to perform frequency-domain triangulation and reconstruct spatial deflection shapes. By introducing additional camera views into the image-based measurement, its field of view is extended and the signal-to-noise ratio of the final result is increased. For linear, time-invariant mechanical structures under stationary excitation, full-field 3D measurements of high-frequency vibrations can be performed using a single still-frame monochrome camera. The proposed method identifies displacements in the frequency domain directly on the camera sensor, resulting in orders-of-magnitude smaller data sizes and post-processing times compared with conventional multiview image-based methods.

Keywords: Spectral Optical Flow Imaging, full-field displacement measurement, single camera, multiview, still camera, frequency domain triangulation

*Corresponding author

Email address: janko.slavic@fs.uni-lj.si (Janko Slavič)

1. Introduction

Image-based displacement measurement methods have long been recognized for their many practical advantages. Their adoption is often only limited by technical aspects of the image-based displacement measurement process [1]. With advances in high-speed imaging technology and high-speed video processing techniques many of these shortcomings have been eliminated, and digital-image processing techniques have become a valid option for highly accurate operational and modal analysis [2].

Image-based methods are particularly well-suited to cases in which a high spatial resolution is required, and the use of conventional transducers is impractical due to problems such as excessive mass-loading, size or obstructed access to the structure under test [3]. Due to the ability to remotely and instantaneously acquire full-field information, image-based techniques are increasingly being used to measure the vibrations of rotating structures by researchers such as Uehara and Sirohi [4], Wu et al. [5] or Poozesh et al. [6]. Structural health monitoring is another field in which image-based techniques are often used [7, 8]. An unmanned aerial vehicle (UAV)-supported setup for wind-turbine monitoring has been presented by Khadka et al. [9]. 3D digital image correlation (DIC) with surface-stitching has been used in applications requiring high spatial resolution and with complex-shaped specimens by Srivastava and Baqersad [10]. Digital image processing methods have been used for precise, high-speed, microscopic displacement tracking with micro-vision [11], and, at the other end of the scale, for remote inspection and monitoring of concrete buildings under seismic vibration [12].

Although numerous different approaches to extracting displacement data from digital images exist, gradient-based techniques are the most commonly used. These methods utilize the principles of optical flow and template matching [13] to estimate the displacements of a high-contrast speckle pattern on the observed surface. DIC [14] is the most established gradient-based method that is widely used for 2D as well as 3D displacement and deformation measurement in experimental mechanics [15]. DIC has long been used for vibration measurement by authors such as Helfrick et al. [16] or Wang et al. [17], while possible improvements to the method remain an important research subject [18, 19]. An alternative gradient-based technique of measuring subpixel displacements for vibration analysis, the Simplified Optical Flow method, offers similar accuracy at a significantly lower numerical load, as demonstrated by Javh et al. [20]. By using a novel dynamic substructuring approach, the accuracy of the obtained FRFs can be further improved, as shown by Bregar et al. [21]. Another quickly evolving area of research is the phase-based approach to displacement identification [22]. Phase-based methods have been used to accurately identify the displacements in structural dynamics by researchers such as Sarafi et al. [23], improve the accuracy of DIC measurements in a combined approach [24], as well as for structural identification through magnified tracking [25]. Machine learning approaches to image-based vibration measurement are also increasingly being used [26].

To extract the spatial information from two-dimensional images using 3D DIC, multiple time-synchronized views of the observed specimen are combined in a triangulation step [27]. This is achieved by a stereo-pair of high-speed cameras, simultaneously acquiring images from slightly different viewpoints, while the stereo system’s field of view remains limited to a single observed face of the specimen, as reported by Patil et al. [28]. The additional time synchronization, feature-matching, imaging system calibration and triangulation steps introduce a new layer of complexity [29] and increase the cost of the imaging setup, while any inaccuracies in the synchronization and optical systems can have an adverse effect on the measurement accuracy [30]. For these reasons, many single-camera multiview approaches have been studied in recent years. These can utilize additional optical devices, such as prisms used by Genovese et al. [31] and mirrors [32, 33] as well as color high-speed cameras and optical filters, as demonstrated by Yu and Pan [34], to effectively project multiple views of the specimen onto a single camera sensor. The fringe-projection technique used by Felipe-Sesé et al. [35] can also be used for single-camera spatial measurements. The frequency-domain triangulation of harmonic motion, recently introduced by Gorjup et al. [36], is an alternative that uses a single, moving high-speed camera to measure the 3D deflection shapes of complex-shaped specimens without any loss of spatial resolution by utilizing the principles of multiview geometry in the frequency domain.

In an effort to reduce the cost and complexity of imaging systems for vibration measurement, as well as to reduce the effects of the low signal-to-noise ratio normally associated with high-speed cameras, various low-frame-rate approaches to high-frequency measurements have also been explored. This can be achieved, for example, by down-sampling in the case of Barone et al. [37] or aliasing, utilized by Yang et al. [38]. By using the recently introduced Spectral Optical Flow Imaging (SOFI) method, which employs a controlled light source to effectively perform an analogous Fourier integral on the image sensor [39], 2D images of the deflection shapes at high frequencies can be produced using only a still monochrome camera [40], while reducing the data size and post-processing times required to measure the displacement spectra in digital images.

In this study, the SOFI method is extended to 3D operating-deflection-shape (ODS) measurements using the frequency-domain triangulation approach [36]. Utilizing the properties of a linear, time-invariant mechanical system under stationary or periodic excitation, spatial vibration measurements of a complex-shaped specimen are performed using only a controlled light source and a single still-frame monochrome camera.

This paper is organised as follows. Sec. 2 gives an overview of the Spectral Optical Flow Imaging method. In Sec. 3, the multiview Spectral Optical Flow Imaging method for 3D deflection shape measurement with frequency-domain triangulation is introduced. Sec. 4 presents the experimental work with results and Sec. 5, the conclusions.

2. Theoretical background of Spectral Optical Flow Imaging

The Spectral Optical Flow Imaging (SOFI) method, introduced in [39], offers a new approach to image-based vibration measurement, using only a still-frame camera and a controlled illumination source to produce frequency-domain deflection shape images. The method is based on the brightness-constancy constraint of optical flow [41]

$$I(\mathbf{u}, t) = I(\mathbf{u} + \Delta\mathbf{u}, t + \Delta t) \quad (1)$$

from which follows the change in the image intensity for small displacements:

$$I(\mathbf{u} + \Delta\mathbf{u}, t) = I(\mathbf{u}, t) + \nabla I(\mathbf{u}) s(t) \quad (2)$$

where $\mathbf{u} = \{u, v\}^T$ is the position of the observed image element (pixel), and $s(t)$ is the displacement in the direction of the local image gradient $\nabla I(\mathbf{u})$.

The intensity values of an image, in turn, are the result of the radiance field $r(\mathbf{u}, L, t) = P(\mathbf{u}, t) L(t)$ of the observed surface with a reflectance pattern $P(\mathbf{u})$ with illumination $L(t)$, integrated on the camera sensor over the exposure time T :

$$I(\mathbf{u}, t) = \int_0^T r(\mathbf{u}, L, t) dt \quad (3)$$

Assuming the illumination is varying harmonically with a static component L_0 and amplitude L_A at frequency ω_l :

$$L(t) = L_0 + L_A \sin(\omega_l t) \quad (4)$$

Eq. (2) can be written in terms of the surface radiance patterns, integrated over the exposure time, to produce [39]:

$$I(\mathbf{u}(t), L(t)) = I(\mathbf{u}, L_0) + \frac{L_A}{L_0} \nabla I(\mathbf{u}, L_0) \frac{S_S(\mathbf{u}, \omega_l)}{2} \quad (5)$$

Here, $S_S(\mathbf{u}, \omega_l)$ is the sinusoidal displacement spectral component at ω_l , which can subsequently be calculated as:

$$S_S(\mathbf{u}, \omega_l) = \frac{I(\mathbf{u}(t), L(t)) - I(\mathbf{u}, L_0)}{\frac{1}{2} \frac{L_A}{L_0} \nabla I(\mathbf{u}, L_0)} \quad (6)$$

where $I(\mathbf{u}(t), L(t))$ is the image of the vibrating object with sinusoidally varying illumination (4), and $I(\mathbf{u}, L_0)$ is the reference image of a steady object under constant illumination with an amplitude L_0 .

Looking at a single pixel, only the displacement spectral component $S_S(\mathbf{u}, \omega_l)$ in the direction of the local image gradient $\nabla I(\mathbf{u})$ can be measured. To measure 2D displacements, a subset-based method such as the Lucas-Kanade image-registration algorithm [13] can be used with the produced SOFI images:

$$\Delta\mathbf{u}_S(\omega_l) = 2 \frac{L_0}{L_A} \left[\begin{array}{cc} \sum \left(\frac{\partial I_0}{\partial u} \right)^2 & \sum \frac{\partial I_0}{\partial u} \frac{\partial I_0}{\partial v} \\ \sum \frac{\partial I_0}{\partial u} \frac{\partial I_0}{\partial v} & \sum \left(\frac{\partial I_0}{\partial v} \right)^2 \end{array} \right]^{-1} \left\{ \begin{array}{c} \sum (I_1 - I_0) \frac{\partial I_0}{\partial u} \\ \sum (I_1 - I_0) \frac{\partial I_0}{\partial v} \end{array} \right\} \quad (7)$$

where I_0 is the reference image $I(\mathbf{u}, L_0)$ and I_1 is the image $I(\mathbf{u}(t), L(t))$.

By changing the phase between the excitation and the harmonically controlled varying illumination $L(t)$ by $\pi/2$ (4), the cosine spectral component amplitude $\Delta\mathbf{u}_C(\omega_l)$ can be measured.

Observing the displacement spectral components at multiple points \mathbf{u} on the imaged surface, the complex ODS image at ω_l can now be constructed by:

$$\Delta\mathbf{u}(\omega_l) = \frac{\Delta\mathbf{u}_C(\omega_l) - j\Delta\mathbf{u}_S(\omega_l)}{2} \quad (8)$$

where j is the imaginary unit.

As the measured frequency ω_l is not dictated by the image-acquisition rate of the camera, but rather by harmonically controlling the light source, the frequency range of the measurement can be very wide, and a still-frame camera can be used for the image acquisition. Since the displacement spectral components are measured by effectively performing an analogue Fourier transform on the camera sensor, the exposure time T should be set to a multiple of the illumination frequency period $2\pi/\omega_l$ to avoid errors due to windowing [39].

3. Multiview SOFI with frequency-domain triangulation for 3D ODSs identification

The proposed spatial deflection shape measurement method has two stages. First, the 2D deflection shape spectral components are measured in multiple camera views (e.g., by moving either the camera or the observed object) using SOFI, as described in Sec. 2. Using this method, deflection shape images at different observed response frequencies (8) can be constructed using only a single still-frame monochrome camera.

In the second stage, introduced in this section, the obtained multiview deflection shape images are input to the frequency-domain triangulation algorithm [36], producing full-field spatial ODSs of the specimen at selected frequencies.

In a multiview imaging setup, a particular view is characterized by a perspective camera matrix \mathbf{P} , describing the optical properties of the camera, as well as its position and orientation in a chosen reference frame:

$$\mathbf{P} = \mathbf{K} [\mathbf{R}|\mathbf{t}] \quad (9)$$

where \mathbf{K} is the calibration matrix of the intrinsic parameters of the optical system, and $[\mathbf{R}|\mathbf{t}]$ is the extrinsic matrix, composed of a rotation matrix \mathbf{R} and a translation vector \mathbf{t} [27], as illustrated in Fig. 1.

The camera matrix \mathbf{P} of a view (or multiple camera matrices, in the case of a multiview setup) is determined by calibrating the imaging system. This is usually achieved by using a series of images of a planar calibration pattern [42] to determine both the intrinsic and extrinsic parameters of a view. Alternatively, the extrinsic parameters in a multiview system can be identified by observing an object of known geometry, matching the locations of chosen geometrical features

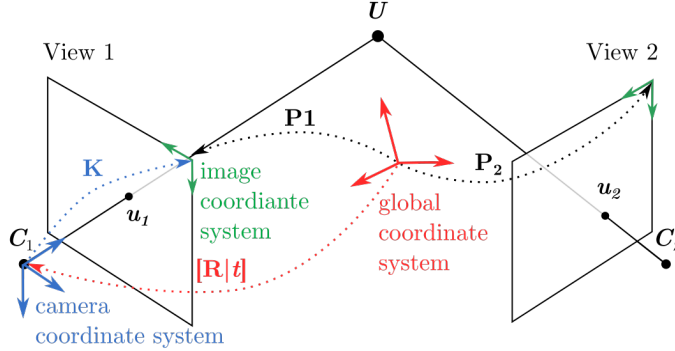


Figure 1: Multiview imaging system and triangulation example.

on the object in multiple views and solving the Perspective-n-Point problem [43] in each of the multiple views.

The 3×4 perspective camera matrix \mathbf{P} describes a projective mapping of any point in space $\mathbf{U} = \{U, V, W, 1\}^T$ to its 2D image $\mathbf{u} = w \{u, v, 1\}^T$ (written in homogeneous coordinates), linear in projective space [27]:

$$\mathbf{u} = \mathbf{P} \mathbf{U} \quad (10)$$

where w is the perspective scale factor:

$$w = \mathbf{p}^3 \mathbf{U} \quad (11)$$

In (11), \mathbf{p}^3 denotes the third row of the perspective camera matrix \mathbf{P} .

The Euclidean representation of the projected image is given by dividing with the perspective scale factor:

$$\mathbf{u} = \frac{1}{w} \mathbf{P} \mathbf{U} \quad (12)$$

making the perspective camera transform non-linear in Euclidean space [27]. Although not a problem in most multiview-imaging applications, this nonlinearity has important implications when attempting to apply the principles of multiple-view geometry to identifying spatial displacements in the frequency domain using image-based measurement methods [36].

As Eq. (12) maps multiple points \mathbf{U} in space into the same image \mathbf{u} , the perspective camera transform is non-invertible. After eliminating the scale factor (11) from the first two equations of (12), identifying the position \mathbf{u} of a single known spatial point \mathbf{U} in a calibrated view gives us two equations, linear in the three unknown coordinates of \mathbf{U} :

$$\begin{aligned} w u &= (\mathbf{p}^3 \mathbf{U}) u = \mathbf{p}^1 \mathbf{U} \\ w v &= (\mathbf{p}^3 \mathbf{U}) v = \mathbf{p}^2 \mathbf{U} \end{aligned} \quad (13)$$

To successfully reconstruct the 3D position of a point \mathbf{U} from the images, we therefore need additional views of the same point in space. With at least two calibrated views of the same geometry, spatial information can be recovered from 2D images using the perspective-camera transform equation (12) in the triangulation process (Fig. 1) [44].

To reconstruct the spatial deflection shapes from the displacements, measured at ω_l using SOFI (2), the deflection-shape images (8) must therefore be related to the 3D deflection shapes $\Delta\mathbf{U}(\omega_l)$ by a perspective-camera transform (12) in the frequency domain. As images are not actually produced on the camera sensor at a particular frequency, but rather at a particular point in time, we start by looking at the image-plane relative displacement of a point in space, moving from its reference position \mathbf{U}^{REF} at time t_0 , to the location $\mathbf{U}(t)$ over the period T in Euclidean space:

$$\Delta\mathbf{u}(t) = \frac{1}{w} \mathbf{P} \mathbf{U}(t) - \frac{1}{w^{\text{REF}}} \mathbf{P} \mathbf{U}^{\text{REF}} \quad (14)$$

Applying the Fourier transform to both sides of Eq. (14), we obtain

$$\Delta\mathbf{u}(\omega_l) = \frac{1}{T} \int_{t_0}^{t_0+T} \left(\frac{1}{w} \mathbf{P} \mathbf{U}(t) - \frac{1}{w^{\text{REF}}} \mathbf{P} \mathbf{U}^{\text{REF}} \right) e^{-j\omega_l t} dt \quad (15)$$

where $T = 2\pi n / \omega_l$ is again chosen to be a multiple of the period of ω_l , to avoid errors in the transformation.

Because the perspective scale factors at the two positions of the observed point in space, w^{REF} and w , are not equal, Eq. (15) does not yet give us the desired relation between the 3D deflection shape and its 2D image. However, by assuming small harmonic displacements, typical for high-frequency vibrations, and translating the measured relative displacements $\Delta\mathbf{u}(\omega_l)$ to their reference positions \mathbf{u}^{REF} , we arrive at the following relation, as shown by Gorjup et al. [36]:

$$\underbrace{\Delta\mathbf{u}(\omega_l) + \mathbf{u}^{\text{REF}}}_{\mathbf{u}(\omega_l)} = \frac{1}{w^{\text{REF}}} \mathbf{P} \left(\underbrace{\Delta\mathbf{U}(\omega_l) + \mathbf{U}^{\text{REF}}}_{\mathbf{U}(\omega_l)} \right) \quad (16)$$

Observing the similarities between Eq. (16) and Eq. (12) we see that $\mathbf{u}(\omega_l)$ and $\mathbf{U}(\omega_l)$ in Eq. (16) are related by a perspective-camera transform. $\mathbf{U}(\omega_l)$ can therefore be obtained from 2D deflection shape images (8) by multiview triangulation, and used to compute the spatial ODS $\Delta\mathbf{U}(\omega_l)$ from (16):

$$\Delta\mathbf{U}(\omega_l) = \mathbf{U}(\omega_l) - \mathbf{U}^{\text{REF}} \quad (17)$$

The reference locations of the observed points \mathbf{U}^{REF} must be known, and can readily be obtained by multiview triangulation of the initial image positions \mathbf{u}^{REF} of the analysed points.

3.1. Multiview SOFI method summary

Multiple SOFI measurements are performed, moving the camera or the observed object to obtain the deflection-shape images from different points of view

at various selected frequencies of interest, controlled by setting the illumination control frequency (Sec. 2). After calibrating the imaging system for each set of multiview SOFI measurements at a particular observed frequency ω_l , the frequency-domain triangulation method is used to produce the spatial deflection shapes of the observed structure.

As with the frequency-domain triangulation method, introduced in [36], linearity and time-invariance of the observed system are assumed. To facilitate the single-camera multiview image-acquisition procedure, stationarity or periodicity of the excitation must also be assured.

The proposed single still-frame camera spatial ODS measurement method can be summarized as follows (Fig. 2):

1. SOFI image acquisition with a moving camera.
2. Multiview imaging-system calibration and point-of-interest selection.
3. SOFI deflection-shape image identification.
4. Frequency-domain multiview triangulation and spatial ODS calculation.

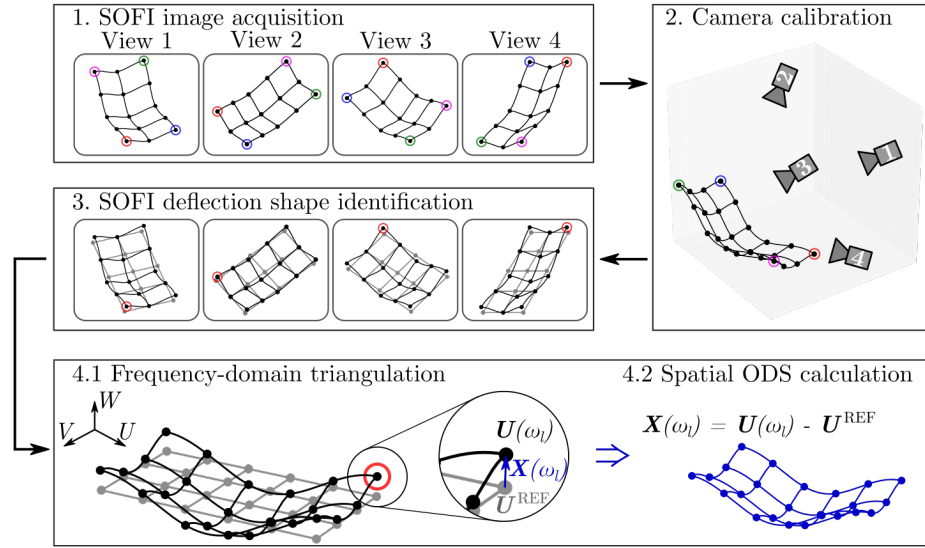


Figure 2: Multiview SOFI with frequency-domain spatial ODS triangulation principle of operation.

4. Experiment and results

To demonstrate the use of the proposed multiview SOFI method, experimental work was conducted to measure the ODSs of a mechanical system. The results, presented in this section, also serve to assess the numerical efficiency and

performance of the method in the presence of random noise in the image-based displacement measurements.

The observed object was a steel 3-plane cubic shell with three symmetrical $120 \text{ mm} \times 120 \text{ mm}$ sides (shown in Fig. 3), fabricated by bending a 1-mm-thick steel sheet-metal plate to form 90-degree angles between the three planes and welded along one seam. A mounting hole 10 mm in diameter was drilled in the center of a chamfered corner approximately 20 mm in altitude at the juncture of the three main planes, forming equal angles with each of them.

The fact that the observed specimen in our experiment was made up of three flat planes was later only used to aid in selecting the same points for analysis in different views. The method is in no way limited by the geometry of the observed object.

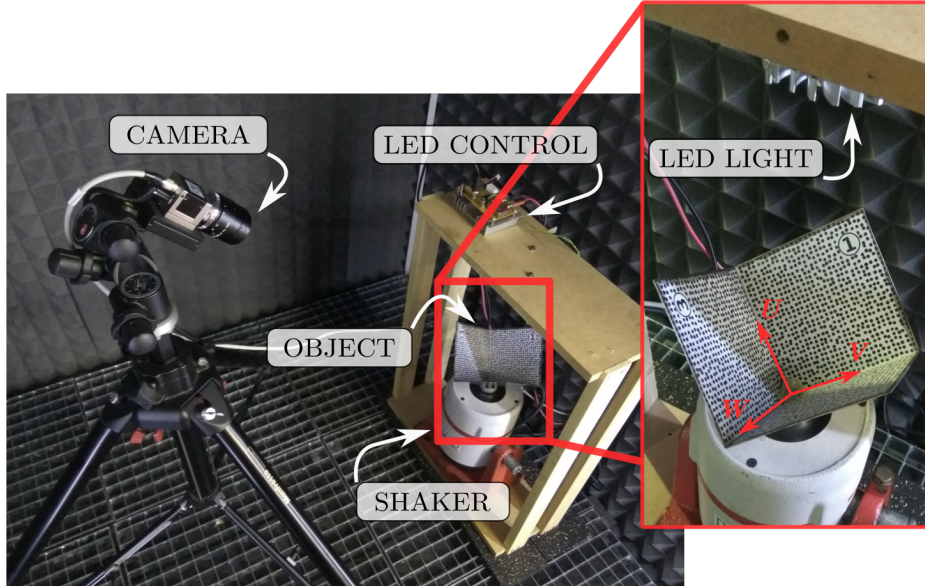


Figure 3: Experimental setup.

To facilitate the optical measurement, a high-contrast speckle pattern was applied to the three inner surfaces of the concave object (Fig. 3).

The 3-plane cubic shell was mounted to a LDS V406 electrodynamic shaker with an M8 mounting bolt through the mounting hole in the chamfered corner face. The object was positioned directly under a LED light source at a distance of approximately 30 cm, oriented at equal angles to the three main planes to achieve uniform illumination. A single monochrome, still-frame Basler acA4112-20um camera was used for the image acquisition. The camera was positioned on a tripod stand, approximately 1200 mm from the coordinate frame's origin at the intersection of the three planes of the observed object, and 25 angular degrees off the shaker's vertical axis (Fig. 3).

A simple FRF measurement of the 3-plane cubic shell was performed first,

using a modal hammer and a 3-axis accelerometer, positioned 10 mm from the outside edges in the corner of one of the three planes. The pyEMA Python library [45] was used to identify the frequencies at which to perform the multi-view SOFI measurements. Four frequencies (146.5 Hz, 285 Hz, 375 Hz and 814 Hz) were selected, each corresponding to a distinct peak in the measured FRF (Fig. 4).

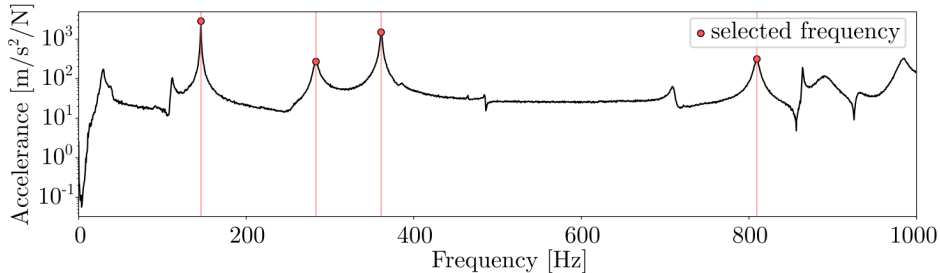


Figure 4: Accelerance FRF of the observed object, used for measurement-frequency selection.

The illumination was proportionally controlled with a sinusoidal signal, generated using a NI9263 module. The shaker control signal was simultaneously generated using the same hardware, and synchronized in terms of frequency to the light control signal and appropriately shifted in phase to produce the SOFI images, required to measure the deflection-shape spectral components at the illumination frequency (Sec. 2). The image acquisition was synchronized to the illumination and excitation control signals by an external hardware trigger, generated by the same NI9263 module. This trigger signal operated the global electronic shutter of the camera, taking the manufacturer-specified exposure delay of 43 μ s into account to ensure synchronization and avoid possible windowing errors. An example of the illumination, shaker and camera exposure control signals in a single SOFI measurement are shown in Fig. 5.

To facilitate the multiview spatial measurements, six different viewpoints of the object were established. The camera was stationary throughout the image-acquisition process, and the shaker assembly with the observed object was rotated 60 degrees around the vertical axis between each measurement session. Fig. 6 shows the reference SOFI images, acquired at the six distinct points of view of the observed 3-plane cubic shell. From each viewpoint, four SOFI measurements were performed by setting the illumination and shaker control signals to one of the selected measurement frequencies. In total, 72 images (4 measurement frequencies \times 6 views \times 3 SOFI images) were acquired at a 12-bit depth and a 4096 \times 3000 pixel resolution, amounting to 1.3 GB of image data. The illumination scaling factor was set to $L_A/L_0 = 0.25/0.75$, and the camera’s exposure time was set to a multiple of the measurement frequency period at approximately 2 s.

The intrinsic parameters of the optical system were first obtained using images of a standard chequerboard calibration pattern. The extrinsic parameters

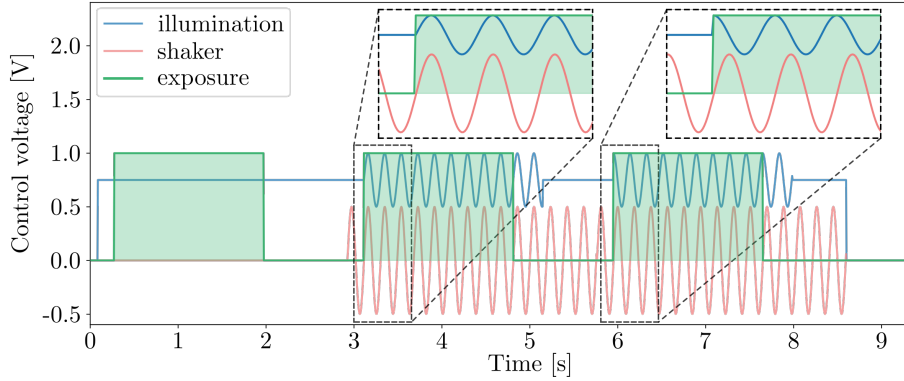


Figure 5: Example illumination, shaker and camera exposure control signals in a single SOFI imaging experiment.

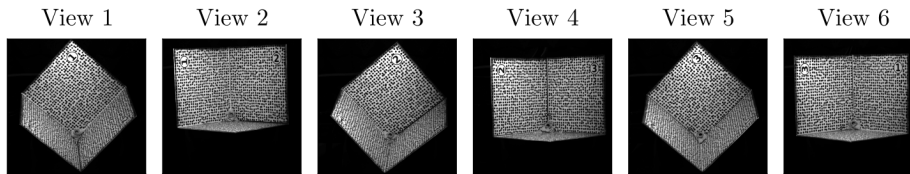


Figure 6: Reference images of a single SOFI multiview measurement.

of the multiview system were computed using the images acquired in the measurement process, so no additional calibration images were required. Fifteen markers with known positions were manually identified in a reference image at each viewpoint, as shown in Fig. 7, and input into the iterative Perspective-n-Point solver, implemented in the OpenCV library [46]. The calibration results - viewpoint positions and orientations in the reference coordinate frame of the measurement - are shown in Fig. 8.

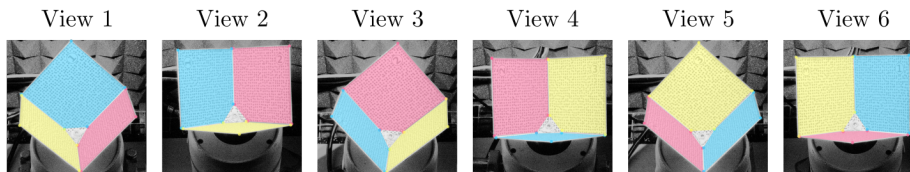


Figure 7: The geometric features of the specimen, located in the reference images for each camera view and used in the extrinsic parameter identification step.

To select the points to be analysed, a regular grid of 56×56 points, offset 10 mm from the outer edges to avoid problems in post processing, was projected onto each of the three visible faces of the 3-plane cubic shell in each reference

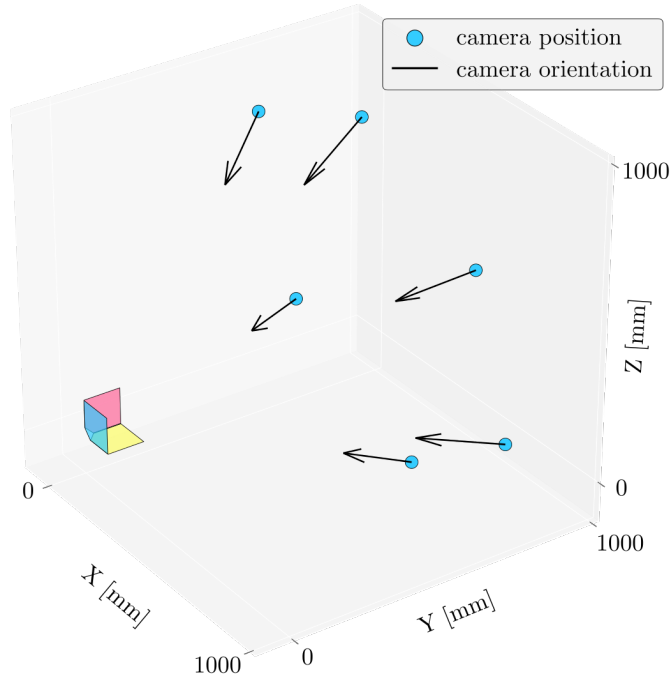


Figure 8: The positions and orientations of the six camera views, resulting from the imaging system calibration step.

image. This resulted in approximately 9000 measurement points in each image. Regions-of-interest, 175×175 pixels in size with the selected points in the center, were analysed using the subset SOFI method, based on the Lucas-Kanade image-registration algorithm (7), to measure the operating deflection shapes at selected frequencies from each of the six distinct points of view. The resulting multiview displacement spectra were input to a linear frequency-domain triangulation algorithm (13) to obtain spatial ODS information.

Spatial ODSs of the 3-plane cubic shell at the four selected measurement frequencies were identified. The acquired ODSs are shown in Fig. 9. Some apparent anomalies can be observed in the result, e.g., at the outer corners of the three planes, where the surface pattern was not optimally suited for gradient-based image processing (Fig. 6). This highlights the importance of surface preparation for image-based measurements. Still, the obtained results closely resemble the expected spatial ODSs of the 3-plane cubic shell, observed in previous experiments on a similar specimen [36].

4.1. Image-based displacement noise and multiview triangulation performance

The frequency-domain multiview triangulation method exhibits high tolerance to noise in the individually identified 2D displacement spectra, resulting from the over-determination of the linear triangulation process when observing

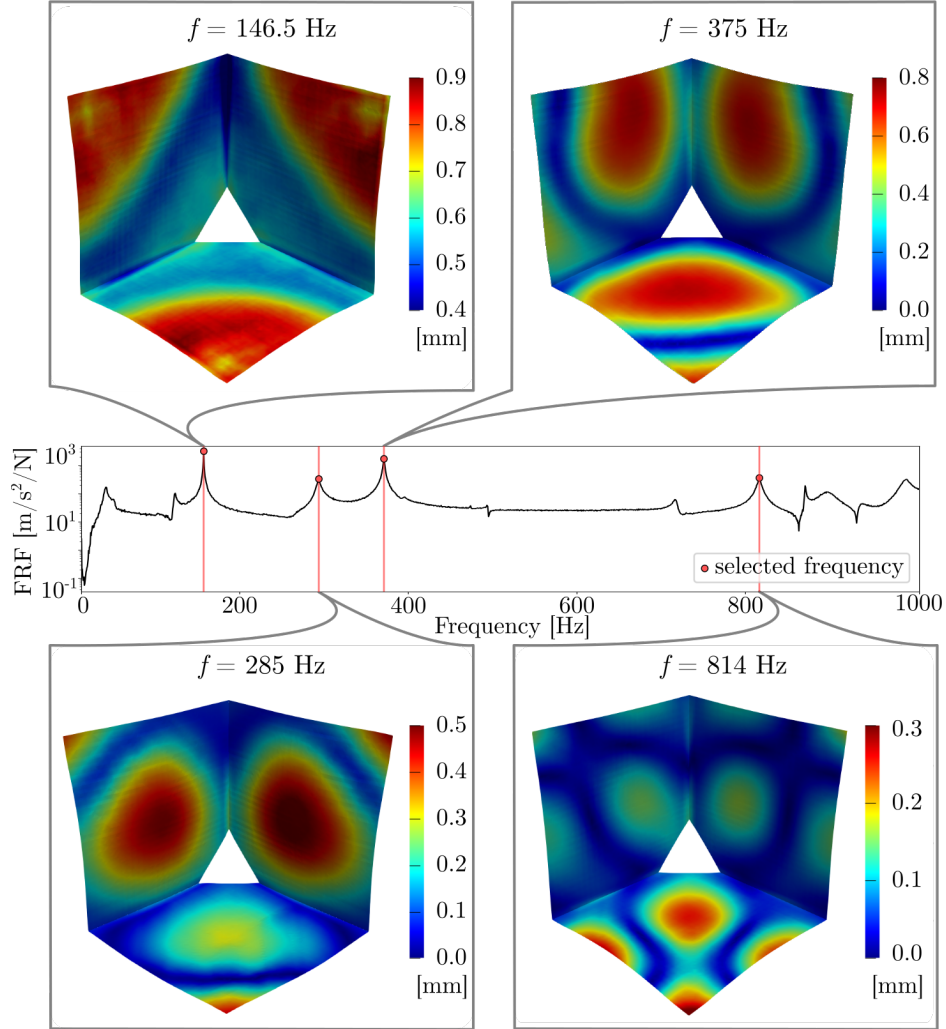


Figure 9: ODS magnitudes, identified using multiview SOFI at four selected measurement frequencies.

each analysed point from a large number of views [27]. This is illustrated in Fig. 10, which shows the relatively noisy SOFI results in six distinct views of the multiview measurement at 814 Hz, and the resulting deflection shape after the multiview triangulation.

The effects of the multiview redundancy were further explored in a series of numerical experiments. The spatial deflection shape, identified at 375 Hz, was projected back into each of the six camera views using Eq. (16). In this way, zero-noise image representations of the 3D deflection shape, corresponding to our imaging system’s configuration, were obtained (see Fig. 11 a). These zero-

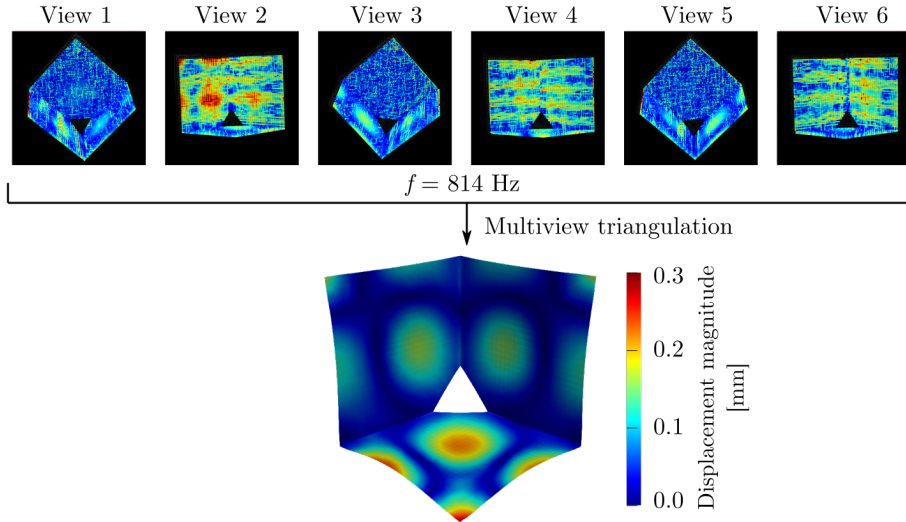


Figure 10: Six displacement spectra images identified in the multiview SOFI measurement at 814 Hz and the resulting spatial ODS.

noise views were artificially corrupted by adding Gaussian random noise. The resulting multiview displacement spectra for additive noise of standard deviation $\sigma_{\text{noise}} = 1.5$ px are shown in Fig. 11 b).

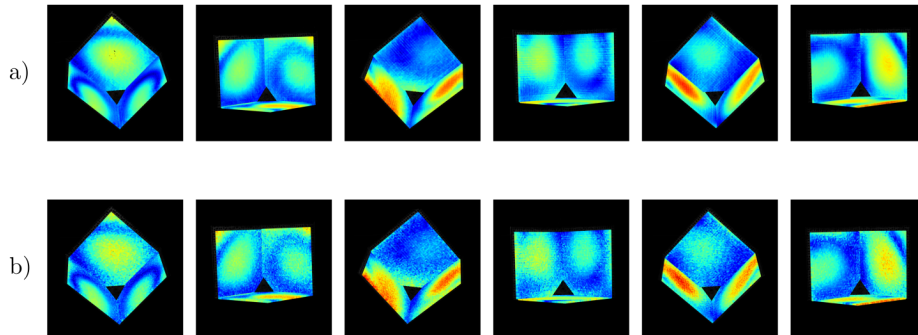


Figure 11: Multiview image spectra with added random noise: a) $\sigma_{\text{noise}} = 0$ px; b) $\sigma_{\text{noise}} = 1.5$ px.

The frequency-domain triangulation procedure was performed twice. First, all six views were included in the triangulation step. The second time, only views 1, 3, and 5 (see Fig. 6) were used for triangulation. Examples of the multiview triangulation results with added noise are shown in Fig. 12. The spatial deflection shape, resulting from these noisy displacement spectra, was compared to the original ODS. In this way, the effects of the number of spectra, in the multiview frequency-domain triangulation on the measurement precision

were observed.

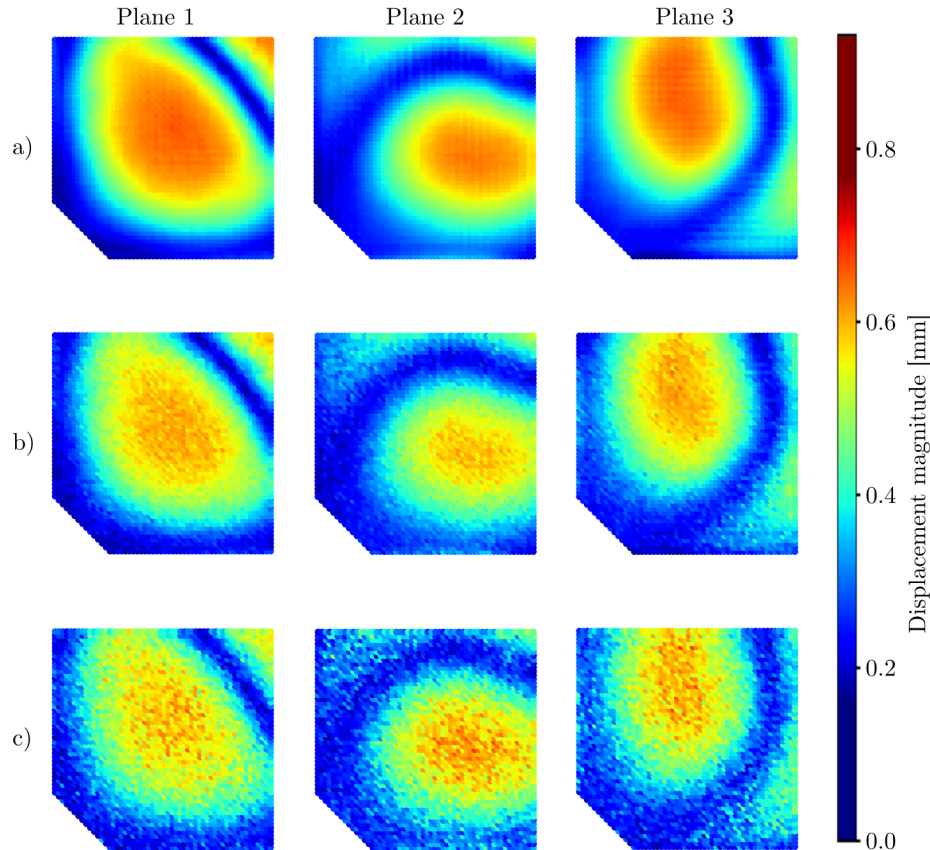


Figure 12: Examples of spatial ODS magnitudes for each plane of the 3-plane cubic shell, obtained by triangulating multiview displacement spectra with added random noise: a) original deflection shape; b) 6-view triangulation, $\sigma_{\text{noise}} = 1.5$ px; c) 3-view triangulation, $\sigma_{\text{noise}} = 1.5$ px.

Applying a similar procedure for different levels of added random noise, the error in the spatial ODS identification at different image-based displacement spectra signal-to-noise-ratios (SNR) was observed. The results are summarized in Tab. 1. A graphical representation of the multiview triangulation error versus the image-based displacement spectra SNR for 3 and 6 camera views is shown in Fig. 13. The obtained results consistently indicate that the robustness to random displacement measurement errors increases with the number of views used for triangulation.

4.2. SOFI and DIC numerical cost comparison

To characterize the numerical effort required to produce image-based displacement spectra using the proposed multiview SOFI method, the analysis

Table 1: Measurement errors due to noise image-based displacement spectra.

SNR [dB]	σ_{noise} [px]	6-view triangulation		3-view triangulation	
		μ_{error} [mm]	σ_{error} [mm]	μ_{error} [mm]	σ_{error} [mm]
∞	0.00	0.00	4.42e-13	0.00	4.16e-13
18.62	0.50	1.59e-03	1.38e-02	3.05e-03	1.94e-02
12.61	1.00	5.98e-03	2.72e-02	1.07e-02	3.80e-02
9.110	1.50	1.17e-02	4.00e-02	2.14e-02	5.67e-02
6.573	2.00	1.92e-02	5.30e-02	3.36e-02	7.44e-02

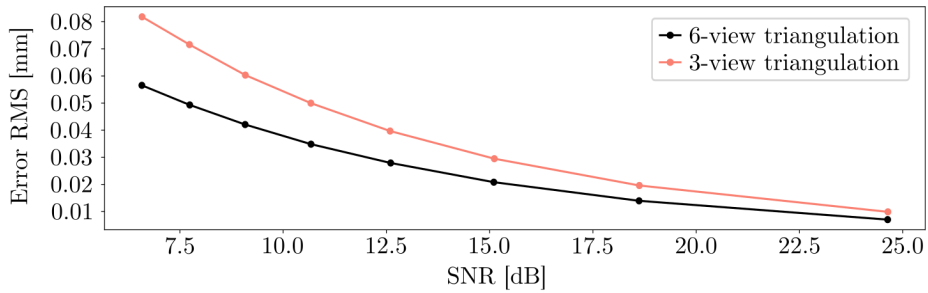


Figure 13: Errors in measurement results due to noisy image-based displacement spectra.

times are compared to a typical DIC-based spatial ODS measurement in the observed frequency range [36].

Both algorithms were implemented in the Python programming language, utilizing the NumPy numerical library to perform the vectorized operations [47]. Displacements of multiple points in the six acquired views were analysed with different subset size settings, and, in the case of DIC, transformed into the frequency domain using FFT, to acquire comparable multiview displacement spectra using both methods. Detailed settings of the DIC measurement are shown in Tab. 2. The presented analysis times were normalized by the total number of points in the six analysed views in both cases.

Table 2: DIC analysis settings.

Setting	Value
Frame rate	10^4
Acquired images	10^4
Image resolution	1024 px \times 1024 px
Image file size	120 GB
Interpolation order	cubic
DIC implementation	Lucas-Kanade, translations only [48]

The actual post-processing times will depend on the analysis settings, as

well as the implementations of the compared algorithms. Still, the results of this comparison, presented in Tab. 3 and Fig. 14, give an insight into the relative numerical cost of both methods.

Similarly, the raw image data sizes will change with different imaging-system settings. Nevertheless, as the displacement spectra are captured directly in the frequency domain, a significant data size reduction is to be expected when using the proposed method.

Table 3: SOFI and DIC analysis times, in seconds per analysed point.

Subset size [px]	SOFI	DIC
	Time per point [s]	
25×25	0.0021	26.708
75×75	0.0027	44.093
125×125	0.0038	81.503
175×175	0.0053	125.30
225×225	0.0076	193.68
275×275	0.0104	270.01

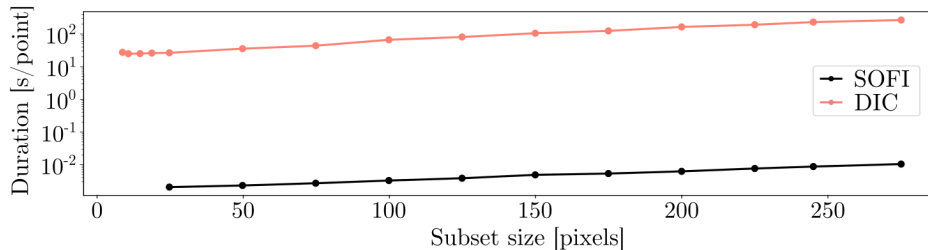


Figure 14: SOFI and DIC analysis times, in seconds per analysed point.

5. Conclusions

The SOFI method for measuring displacement spectral components was extended to facilitate multiview measurements of spatial displacement spectra. The novel approach utilizes the frequency-domain triangulation method for small harmonic motion to measure spatial ODSs using a still-frame monochrome camera for image acquisition. The proposed method was demonstrated in an experiment to measure the 3D ODSs of a mechanical structure. This indicates that the resulting 3D displacement spectra can be used in vibration measurements. The method is limited to experimental analysis of linear, time-invariant mechanical structures in stationary vibrations. Precise control of the illumination and a suitable surface preparation are required to achieve reliable results.

Under these conditions, the proposed method exhibits a high tolerance to the random noise of the displacement measurements in individual camera views.

This observation is further explored in a numerical experiment, which shows that the adverse effects of a low signal-to-noise ratio of image-based displacement measurements are mitigated by including more camera views in the frequency-domain triangulation procedure. This is advantageous in image-based measurements due to the high level of random noise (relative to conventional vibration measurement methods) inherently present in digital images.

As a still-frame camera is used for image acquisition and the measurement frequency is only influenced by the harmonically pulsating illumination, the upper measurement frequency of the multiview SOFI method is not limited by the frame-rate of the camera. The performance at higher frequencies is, however, still subject to the issues normally associated with image-based methods, caused by low displacement magnitudes.

Another advantage of the introduced multiview SOFI method compared to conventional image-based techniques of measuring displacement spectra is the numerical efficiency of the proposed method's post-processing stage. After identifying the frequencies of interest in an additional broadband FRF measurement step, SOFI readily produces displacement spectral components by performing the Fourier transform on the camera sensor. As a result, the amount of recorded image data is significantly decreased (by approximately two orders of magnitude in our case), and the numerical effort to obtain multiview displacement spectra is approximately four orders of magnitude lower than for conventional methods. This is demonstrated in a comparison of the required computation times of multiview SOFI with a typical DIC measurement.

Especially for specimens with complex geometry, the multiview SOFI method offers a promising, cost-effective and efficient approach to extending the field of view of image-based measurements. It enables high-frequency spatial vibration measurement using a single, still-frame camera, without reducing the high spatial resolution associated with image-based measurements.

Acknowledgement

The authors acknowledge the partial financial support from the Slovenian Research Agency (research core funding no. P2-0263 and project J2-1730).

References

- [1] T. J. Bebernis, D. A. Ehrhardt, High-speed 3D digital image correlation vibration measurement: Recent advancements and noted limitations, *Mechanical Systems and Signal Processing* 86 (2017) 35 – 48, full-field, non-contact vibration measurement methods: comparisons and applications. doi:<https://doi.org/10.1016/j.ymssp.2016.04.014>.
URL <http://www.sciencedirect.com/science/article/pii/S0888327016300528>
- [2] J. Javh, J. Slavič, M. Boltežar, High frequency modal identification on noisy high-speed camera data, *Mechanical Systems and Signal Processing* 98 (2018) 344 – 351. doi:<https://doi.org/10.1016/j.ymssp.2017.05.008>.
URL <http://www.sciencedirect.com/science/article/pii/S0888327017302637>
- [3] J. Baqersad, P. Poozesh, C. Niezrecki, P. Avitabile, Photogrammetry and optical methods in structural dynamics – a review, *Mechanical Systems and Signal Processing* 86 (2017) 17 – 34, full-field, non-contact vibration measurement methods: comparisons and applications. doi:<https://doi.org/10.1016/j.ymssp.2016.02.011>.
URL <http://www.sciencedirect.com/science/article/pii/S0888327016000388>
- [4] D. Uehara, J. Sirohi, Full-field optical deformation measurement and operational modal analysis of a flexible rotor blade, *Mechanical Systems and Signal Processing* 133 (2019) 106265. doi:<https://doi.org/10.1016/j.ymssp.2019.106265>.
URL <http://www.sciencedirect.com/science/article/pii/S0888327019304807>
- [5] R. Wu, D. Zhang, Q. Yu, Y. Jiang, D. Arola, Health monitoring of wind turbine blades in operation using three-dimensional digital image correlation, *Mechanical Systems and Signal Processing* 130 (2019) 470 – 483. doi:<https://doi.org/10.1016/j.ymssp.2019.05.031>.
URL <http://www.sciencedirect.com/science/article/pii/S0888327019303401>
- [6] P. Poozesh, A. Sabato, A. Sarrafi, C. Niezrecki, P. Avitabile, R. Yarala, Multicamera measurement system to evaluate the dynamic response of utility-scale wind turbine blades, *Wind Energy* 23 (7) (2020) 1619–1639. arXiv:<https://onlinelibrary.wiley.com/doi/pdf/10.1002/we.2505>, doi:10.1002/we.2505.
URL <https://onlinelibrary.wiley.com/doi/abs/10.1002/we.2505>
- [7] J. Lee, K.-C. Lee, S. Jeong, Y.-J. Lee, S.-H. Sim, Long-term displacement measurement of full-scale bridges using camera ego-motion compensation, *Mechanical Systems and Signal Processing* 140 (2020) 106651.

- doi:<https://doi.org/10.1016/j.ymsp.2020.106651>.
URL <http://www.sciencedirect.com/science/article/pii/S0888327020300376>
- [8] C.-Z. Dong, F. N. Catbas, A review of computer vision-based structural health monitoring at local and global levels, *Structural Health Monitoring* 0 (0) (0) 1475921720935585. arXiv:<https://doi.org/10.1177/1475921720935585>, doi:10.1177/1475921720935585.
URL <https://doi.org/10.1177/1475921720935585>
- [9] A. Khadka, B. Fick, A. Afshar, M. Tavakoli, J. Baqersad, Non-contact vibration monitoring of rotating wind turbines using a semi-autonomous uav, *Mechanical Systems and Signal Processing* 138 (2020) 106446. doi:<https://doi.org/10.1016/j.ymsp.2019.106446>.
URL <http://www.sciencedirect.com/science/article/pii/S0888327019306673>
- [10] V. Srivastava, J. Baqersad, An optical-based technique to obtain operating deflection shapes of structures with complex geometries, *Mechanical Systems and Signal Processing* 128 (2019) 69 – 81. doi:<https://doi.org/10.1016/j.ymsp.2019.03.021>.
URL <http://www.sciencedirect.com/science/article/pii/S0888327019301955>
- [11] H. Li, B. Zhu, Z. Chen, X. Zhang, Realtime in-plane displacements tracking of the precision positioning stage based on computer micro-vision, *Mechanical Systems and Signal Processing* 124 (2019) 111 – 123. doi:<https://doi.org/10.1016/j.ymsp.2019.01.046>.
URL <http://www.sciencedirect.com/science/article/pii/S0888327019300627>
- [12] C.-Y. Chang, C.-W. Huang, Non-contact measurement of inter-story drift in three-layer rc structure under seismic vibration using digital image correlation, *Mechanical Systems and Signal Processing* 136 (2020) 106500. doi:<https://doi.org/10.1016/j.ymsp.2019.106500>.
URL <http://www.sciencedirect.com/science/article/pii/S0888327019307216>
- [13] B. D. Lucas, T. Kanade, An iterative image registration technique with an application to stereo vision, in: *Proceedings of the 7th International Joint Conference on Artificial Intelligence - Volume 2, IJCAI'81*, Morgan Kaufmann Publishers Inc., San Francisco, CA, USA, 1981, pp. 674–679.
URL <http://dl.acm.org/citation.cfm?id=1623264.1623280>
- [14] T. C. Chu, W. F. Ranson, M. A. Sutton, Applications of digital-image-correlation techniques to experimental mechanics, *Experimental Mechanics* 25 (3) (1985) 232–244. doi:10.1007/BF02325092.
URL <https://doi.org/10.1007/BF02325092>

- [15] B. Pan, Digital image correlation for surface deformation measurement: historical developments, recent advances and future goals, *Measurement Science and Technology* 29 (8) (2018) 082001.
URL <http://stacks.iop.org/0957-0233/29/i=8/a=082001>
- [16] M. N. Helfrick, C. Niezrecki, P. Avitabile, T. Schmidt, 3D digital image correlation methods for full-field vibration measurement, *Mechanical Systems and Signal Processing* 25 (3) (2011) 917 – 927. doi:<https://doi.org/10.1016/j.ymsp.2010.08.013>.
URL <http://www.sciencedirect.com/science/article/pii/S0888327010002980>
- [17] W. Wang, J. E. Mottershead, T. Siebert, A. Pipino, Frequency response functions of shape features from full-field vibration measurements using digital image correlation, *Mechanical Systems and Signal Processing* 28 (2012) 333 – 347, *interdisciplinary and Integration Aspects in Structural Health Monitoring*. doi:<https://doi.org/10.1016/j.ymsp.2011.11.023>.
URL <http://www.sciencedirect.com/science/article/pii/S0888327011005152>
- [18] Y.-H. Chang, W. Wang, T. Siebert, J.-Y. Chang, J. E. Mottershead, Basis-updating for data compression of displacement maps from dynamic DIC measurements, *Mechanical Systems and Signal Processing* 115 (2019) 405 – 417. doi:<https://doi.org/10.1016/j.ymsp.2018.05.058>.
URL <http://www.sciencedirect.com/science/article/pii/S0888327018303170>
- [19] L. Wang, S. Bi, H. Li, Y. Gu, C. Zhai, Fast initial value estimation in digital image correlation for large rotation measurement, *Optics and Lasers in Engineering* 127 (2020) 105838. doi:<https://doi.org/10.1016/j.optlaseng.2019.105838>.
URL <http://www.sciencedirect.com/science/article/pii/S014381661930449X>
- [20] J. Javh, J. Slavič, M. Boltežar, The subpixel resolution of optical-flow-based modal analysis, *Mechanical Systems and Signal Processing* 88 (2017) 89 – 99. doi:<https://doi.org/10.1016/j.ymsp.2016.11.009>.
URL <http://www.sciencedirect.com/science/article/pii/S0888327016304770>
- [21] T. Bregar, K. Zaletelj, G. Čepon, J. Slavič, M. Boltežar, Full-field frf estimation from noisy high-speed-camera data using a dynamic substructuring approach, *Mechanical Systems and Signal Processing* 150 (2021) 107263. doi:<https://doi.org/10.1016/j.ymsp.2020.107263>.
URL <http://www.sciencedirect.com/science/article/pii/S088832702030649X>
- [22] N. Wadhwa, M. Rubinstein, F. Durand, W. T. Freeman, Phase-based video motion processing, *ACM Trans. Graph.* 32 (4) (Jul. 2013). doi:10.1145/

2461912.2461966.

URL <https://doi.org/10.1145/2461912.2461966>

- [23] A. Sarrafi, Z. Mao, C. Niezrecki, P. Poozesh, Vibration-based damage detection in wind turbine blades using phase-based motion estimation and motion magnification, *Journal of Sound and Vibration* 421 (2018) 300 – 318. doi:<https://doi.org/10.1016/j.jsv.2018.01.050>.
URL <http://www.sciencedirect.com/science/article/pii/S0022460X18300725>
- [24] P. Poozesh, A. Sarrafi, Z. Mao, P. Avitabile, C. Niezrecki, Feasibility of extracting operating shapes using phase-based motion magnification technique and stereo-photogrammetry, *Journal of Sound and Vibration* 407 (2017) 350 – 366. doi:<https://doi.org/10.1016/j.jsv.2017.06.003>.
URL <http://www.sciencedirect.com/science/article/pii/S0022460X17304698>
- [25] Y. E. Harmanci, U. Gülan, M. Holzner, E. Chatzi, A novel approach for 3d-structural identification through video recording: Magnified tracking, *Sensors (Basel, Switzerland)* 19 (5) (2019) 1229. doi:[10.3390/s19051229](https://doi.org/10.3390/s19051229).
URL <https://doi.org/10.3390/s19051229>
- [26] R. Yang, S. K. Singh, M. Tavakkoli, N. Amiri, Y. Yang, M. A. Karami, R. Rai, Cnn-lstm deep learning architecture for computer vision-based modal frequency detection, *Mechanical Systems and Signal Processing* 144 (2020) 106885. doi:<https://doi.org/10.1016/j.ymsp.2020.106885>.
URL <http://www.sciencedirect.com/science/article/pii/S0888327020302715>
- [27] R. Hartley, A. Zisserman, *Multiple View Geometry in Computer Vision*, 2nd Edition, Cambridge University Press, New York, NY, USA, 2003.
- [28] K. Patil, J. Baqersad, A. Sheidaei, A multi-view digital image correlation for extracting mode shapes of a tire, in: J. M. Harvie, J. Baqersad (Eds.), *Shock & Vibration, Aircraft/Aerospace, Energy Harvesting, Acoustics & Optics*, Volume 9, Springer International Publishing, Cham, 2017, pp. 211–217.
- [29] A. Sabato, N. A. Valente, C. Niezrecki, Development of a camera localization system for three-dimensional digital image correlation camera triangulation, *IEEE Sensors Journal* 20 (19) (2020) 11518–11526.
- [30] B. Pan, L. Yu, Q. Zhang, Review of single-camera stereo-digital image correlation techniques for full-field 3D shape and deformation measurement, *Science China Technological Sciences* 61 (1) (2018) 2–20. doi:[10.1007/s11431-017-9090-x](https://doi.org/10.1007/s11431-017-9090-x).
URL <https://doi.org/10.1007/s11431-017-9090-x>

- [31] K. Genovese, L. Casaletto, J. Rayas, V. Flores, A. Martinez, Stereo-digital image correlation (DIC) measurements with a single camera using a biprism, *Optics and Lasers in Engineering* 51 (3) (2013) 278 – 285. doi:<https://doi.org/10.1016/j.optlaseng.2012.10.001>.
URL <http://www.sciencedirect.com/science/article/pii/S0143816612002837>
- [32] L. Yu, B. Pan, Single-camera high-speed stereo-digital image correlation for full-field vibration measurement, *Mechanical Systems and Signal Processing* 94 (2017) 374 – 383. doi:<https://doi.org/10.1016/j.ymsp.2017.03.008>.
URL <http://www.sciencedirect.com/science/article/pii/S088832701730122X>
- [33] T. Durand-Texte, E. Simonetto, S. Durand, M. Melon, M.-H. Moulet, Vibration measurement using a pseudo-stereo system, target tracking and vision methods, *Mechanical Systems and Signal Processing* 118 (2019) 30 – 40. doi:<https://doi.org/10.1016/j.ymsp.2018.08.049>.
URL <http://www.sciencedirect.com/science/article/pii/S0888327018305934>
- [34] L. Yu, B. Pan, Full-frame, high-speed 3D shape and deformation measurements using stereo-digital image correlation and a single color high-speed camera, *Optics and Lasers in Engineering* 95 (2017) 17 – 25. doi:<https://doi.org/10.1016/j.optlaseng.2017.03.009>.
URL <http://www.sciencedirect.com/science/article/pii/S014381661730060X>
- [35] L. Felipe-Sesé, Ángel J. Molina-Viedma, E. López-Alba, F. A. Díaz, Fp+dic for low-cost 3d full-field experimental modal analysis in industrial components, *Mechanical Systems and Signal Processing* 128 (2019) 329 – 339. doi:<https://doi.org/10.1016/j.ymsp.2019.04.004>.
URL <http://www.sciencedirect.com/science/article/pii/S0888327019302377>
- [36] D. Gorjup, J. Slavič, M. Boltežar, Frequency domain triangulation for full-field 3d operating-deflection-shape identification, *Mechanical Systems and Signal Processing* 133 (2019) 106287. doi:<https://doi.org/10.1016/j.ymsp.2019.106287>.
URL <http://www.sciencedirect.com/science/article/pii/S0888327019305023>
- [37] S. Barone, P. Neri, A. Paoli, A. V. Razonale, Low-frame-rate single camera system for 3d full-field high-frequency vibration measurements, *Mechanical Systems and Signal Processing* 123 (2019) 143 – 152. doi:<https://doi.org/10.1016/j.ymsp.2019.01.016>.
URL <http://www.sciencedirect.com/science/article/pii/S0888327019300147>

- [38] Y. Yang, C. Dorn, T. Mancini, Z. Talken, S. Nagarajaiah, G. Kenyon, C. Farrar, D. Mascareñas, Blind identification of full-field vibration modes of output-only structures from uniformly-sampled, possibly temporally-aliased (sub-nyquist), video measurements, *Journal of Sound and Vibration* 390 (2017) 232 – 256. doi:<https://doi.org/10.1016/j.jsv.2016.11.034>.
URL <http://www.sciencedirect.com/science/article/pii/S0022460X16306897>
- [39] J. Javh, J. Slavič, M. Boltežar, Measuring full-field displacement spectral components using photographs taken with a DSLR camera via an analogue fourier integral, *Mechanical Systems and Signal Processing* 100 (2018) 17 – 27. doi:<https://doi.org/10.1016/j.ymsp.2017.07.024>.
URL <http://www.sciencedirect.com/science/article/pii/S0888327017303898>
- [40] J. Javh, J. Slavič, M. Boltežar, Experimental modal analysis on full-field dslr camera footage using spectral optical flow imaging, *Journal of Sound and Vibration* 434 (2018) 213 – 220. doi:<https://doi.org/10.1016/j.jsv.2018.07.046>.
URL <http://www.sciencedirect.com/science/article/pii/S0022460X18304905>
- [41] B. K. Horn, B. G. Schunck, Determining optical flow, *Artificial Intelligence* 17 (1) (1981) 185 – 203. doi:[https://doi.org/10.1016/0004-3702\(81\)90024-2](https://doi.org/10.1016/0004-3702(81)90024-2).
URL <http://www.sciencedirect.com/science/article/pii/0004370281900242>
- [42] Z. Zhang, A flexible new technique for camera calibration, *IEEE Transactions on Pattern Analysis and Machine Intelligence* 22 (11) (2000) 1330–1334. doi:10.1109/34.888718.
- [43] F. Moreno-Noguer, V. Lepetit, P. Fua, Accurate non-iterative o(n) solution to the PnP problem, 2007 Ieee 11Th International Conference On Computer Vision, Vols 1-6 (2007) 2252–2259.
URL <http://infoscience.epfl.ch/record/179767>
- [44] R. I. Hartley, P. Sturm, Triangulation, *Computer Vision and Image Understanding* 68 (2) (1997) 146 – 157. doi:<https://doi.org/10.1006/cviu.1997.0547>.
URL <http://www.sciencedirect.com/science/article/pii/S1077314297905476>
- [45] K. Zaletelj, T. Bregar, D. Gorjup, J. Slavič, *ladisk/pyema: v0.24* (Sep. 2020). doi:10.5281/zenodo.4016671.
URL <https://doi.org/10.5281/zenodo.4016671>

- [46] OpenCV, Open Source Computer Vision Library, <https://github.com/opencv/opencv> (2018).
- [47] C. R. Harris, K. J. Millman, S. J. van der Walt, R. Gommers, P. Virtanen, D. Cournapeau, E. Wieser, J. Taylor, S. Berg, N. J. Smith, R. Kern, M. Picus, S. Hoyer, M. H. van Kerkwijk, M. Brett, A. Haldane, J. F. del Río, M. Wiebe, P. Peterson, P. Gérard-Marchant, K. Sheppard, T. Reddy, W. Weckesser, H. Abbasi, C. Gohlke, T. E. Oliphant, Array programming with NumPy, *Nature* 585 (7825) (2020) 357–362. doi:10.1038/s41586-020-2649-2.
URL <https://doi.org/10.1038/s41586-020-2649-2>
- [48] K. Zaletelj, D. Gorjup, J. Slavič, *ladisk/pyidi*: Release of the version v0.23 (Sep. 2020). doi:10.5281/zenodo.4017153.
URL <https://doi.org/10.5281/zenodo.4017153>